ELSEVIER

Journal of Fluids and Structures 22 (2006) 315–326

JOURNAL OF FLUIDS AND STRUCTURES

www.elsevier.com/locate/jfs

# Numerical simulations of flow-field interactions between moving and stationary objects in idealized street canyon settings

J.Y. Xia[a], D.Y.C. Leung[b,*], M.Y. Hussaini[a]

[a]*School of Computational Science and Information Technology, The Florida State University, Tallahassee, FL 32306-4120, USA*
[b]*Department of Mechanical Engineering, the University of Hong Kong, Pokfulam Road, Hong Kong*

Received 9 March 2005; accepted 27 December 2005
Available online 28 February 2006

**Abstract**

Numerical simulations of an ideal model of street canyons with moving objects in the horizontal plane were conducted. The simulations were based on the unsteady two-dimensional incompressible Navier–Stokes equations, discretized on an overlapping grid with a numerical scheme that is second-order accurate in both space and time. The computational domain consists of a rectangular background with eight fixed objects arranged in two parallel columns representing the street canyon. Four identical objects were put in each column equidistantly. One or two identical objects were moving along the symmetry line of the computational domain. The objects were either circular or rectangular with rounded corners in shape. The numerical method was first validated by comparing with existing experimental and simulation data. A parametric study was carried out to investigate the influence of the characteristic parameters (such as canyon width, velocity of the moving objects, and separation distance between them) on the wake of the moving objects.


*Keywords:* Navier–Stokes equations; Overlapping grid; High-order finite-difference method

## 1. Introduction

Despite significant improvements in fuel and engine technology, vehicular emissions still dominate the present-day urban environments. In urban environments, especially those areas where population and traffic densities are relatively high, human exposure to toxic substances emitted from vehicles has increased tremendously in recent decades. This is often the case near busy traffic lanes in city centers, where urban topography and microclimate may contribute to the creation of poor natural ventilation, escalating pollution hot spots. High pollution levels have been observed in urban streets flanked by clusters of buildings on both sides. Within these street canyons, pedestrians, drivers and residents are likely exposed to pollutant concentrations exceeding current air quality standards.

Dispersion of vehicular exhaust emissions has recently received considerable attention. A number of pollutant dispersion models have been developed, from Gaussian plume models in 1970s such as CALINE (Beaton et al., 1972)

*Corresponding author. Tel.: +852 2859 7911; fax: +852 2858 5415.
*E-mail address:* ycleung@hku.hk (D.Y.C. Leung).

0889-9746/$ - see front matter 
doi:10.1016/j.jfluidstructs.2005.12.003

and HIWAY (Zimmerman and Thompson, 1975), to differential equation models in 1980s such as ROADWAY (Eskridge and Thompson, 1982). However, most air dispersion models treat the source of traffic pollutants as simple line sources of pollutant, which is obviously a major simplification of the actual situation of a large number of moving point sources. Only a few dispersion models are applicable to urban street environments. Since the 1990s, computational fluid dynamic (CFD) techniques have been employed increasingly in studying street canyon flows [see Vardoulakis et al. (2003) for a review]. Theodoridis and Moussiopoulos (2000) investigated the influence of building density and roof shape on the wind and dispersion characteristics in an urban area. Xia and Leung (2001a–c) studied the flow-fields in street canyons with different building configurations, while Liu et al. (2005) computed the air and pollutant exchange rate in street canyons with different configurations. These studies purely focused on building configuration and its effect on flow regimes in street canyons, but did not include any ground vehicular sources. It has been acknowledged that the wakes of ground vehicles have a significant effect on the dispersion of vehicle-emitted pollutants. Baker (2001) studied the flow velocities and the dispersion of pollutants in the wake of a number of different types of ground vehicles. But the ground vehicles are not situated in street canyons. Ahmad et al. (2002) conducted wind tunnel experiments to investigate dispersion of vehicular pollutants under different urban street configurations. There have few numerical studies of pollutant dispersion behavior in vehicle wakes in street canyons. The complexity of the problem requires a synergistic approach, so that experimental and theoretical results verify each other.

The present paper simulates the flow-field around moving objects in a street canyon, taking into account the interaction between the complex flow regime in street canyons and vehicle wakes. Software package Overture (http://www.llnl.gov/CASC/Overture) is used to solve the Navier–Stokes equations on overlapping grids. The numerical methodology is first validated in the case of flow past a pair of side-by-side identical circular cylinders, for which some experimental results are available (Jester and Kallinderis, 2003). Then we consider two-dimensional flows in a horizontal plane over identical buildings with different configurations. Two sets of numerical simulations are conducted to get an understanding of the flow structure around moving objects. In the first case, simulations of a circular object moving between fixed circular objects in the $x$–$y$ plane is conducted to obtain the unsteady flow-field around the moving and fixed circular objects. In the second set, the geometry is similar to the first set, except that rounded-rectangular objects replace the circular ones. The characteristic parameters are the vehicle speed, the canyon width, and the distance between the moving objects. The effect of these parameters on the street canyon flow-fields was studied.

## 2. Computational model and solution technique

### 2.1. Computational model

The target street canyon was modelled by a rectangular domain with eight fixed circular objects in the horizontal $x$–$y$ plane, which were arranged in two parallel arrays aligned with the wind direction, and one or two moving cylinders along the symmetry line (Fig. 1).

The problem under consideration was a two-dimensional unsteady low-speed flow, and thus governed by the following dimensionless incompressible Navier–Stokes equations:

$$\frac{\partial u}{\partial x}+\frac{\partial v}{\partial y}=0, \tag{1a}$$

$$\frac{\partial u}{\partial t}+u\frac{\partial u}{\partial x}+v\frac{\partial u}{\partial y}=-\frac{\partial p}{\partial x}+\frac{1}{\mathrm{Re}}\left(\frac{\partial^2 u}{\partial x^2}+\frac{\partial^2 u}{\partial y^2}\right), \tag{1b}$$

$$\frac{\partial v}{\partial t}+u\frac{\partial v}{\partial x}+v\frac{\partial v}{\partial y}=-\frac{\partial p}{\partial y}+\frac{1}{\mathrm{Re}}\left(\frac{\partial^2 v}{\partial x^2}+\frac{\partial^2 v}{\partial y^2}\right), \tag{1c}$$

where the velocity components ($u$, $v$) were made nondimensional with respect to the inflow velocity, $U_o$, the Cartesian coordinates $x$ and $y$ with respect to the characteristic width $D$ of the moving object, the time $t$ with respect to $D/U_o$, and pressure, $p$, with respect to the dynamic head. The nondimensional parameters Re is the Reynolds number defined as $\mathrm{Re}=U_oD/v$, where $v$ denotes the kinematic viscosity.

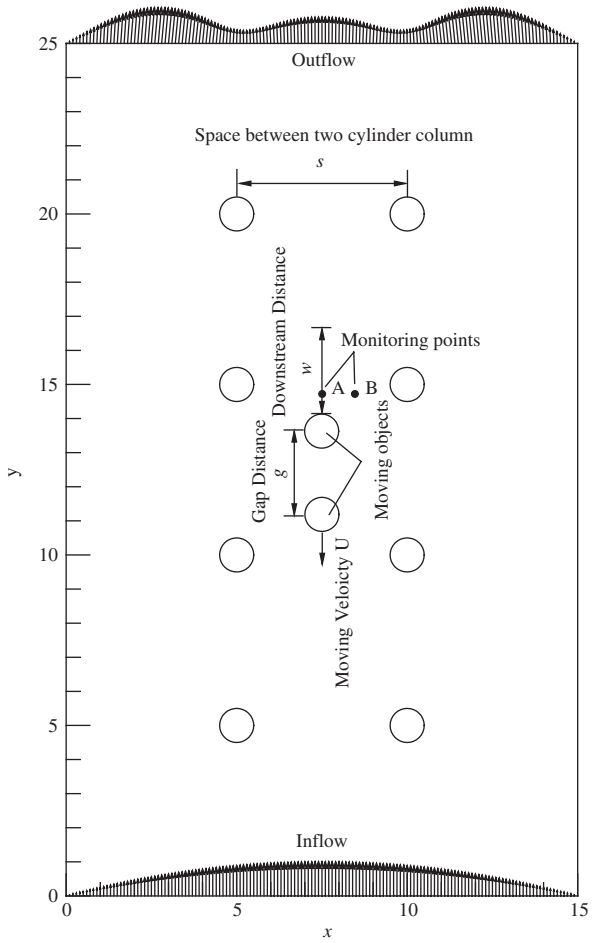


Fig. 1. Computational domain and terms used in present simulations.

For convenience of numerical implementation, the incompressible Navier–Stokes equations are expressed in pressure-Poisson system in vector form as follows:

$$\mathbf{u}_t + (\mathbf{u}\cdot\nabla)\mathbf{u} + \nabla p - \nu\Delta\mathbf{u} - \mathbf{f} = \mathbf{0}, \tag{2a}$$

$$\Delta p + \nabla\cdot[(\mathbf{u}\cdot\nabla)\mathbf{u}] - C_d\nabla\cdot\mathbf{u} - \nabla\cdot\mathbf{f} = 0. \tag{2b}$$

The form of the divergence damping term $C_d\nabla\cdot\mathbf{u}$ appearing in the equation for the pressure will be discussed in next section.

### 2.2. Boundary conditions

A parabolic velocity profile was set at the upstream boundary of the rectangular computational domain with maximum velocity $U_o$ at the symmetric line and zero at the boundary. The downstream boundary was set as outflow, where the velocity was quadratically extrapolated and a mixed derivative of $p$, i.e. $0.1p + \partial_n p = 0$, was used in the present study. Nonslip conditions are applied on the sidewalls of the computational domain and the surface of objects.

## 3. Solution technique

Details of the numerical algorithm for the solution of incompressible Navier–Stokes equations on overlapping grids can be found in Henshaw (1994). For the sake of completeness, we provide here a brief description of the numerical algorithm.

### 3.1. The overlapping grid

The basic idea of the overlapping-grid technique is to partition the domain into a number of topologically simple distinct components, so that grids can then be generated independently for each component and the relevant equations discretized efficiently and accurately thereon. The overlap must be sufficiently large and the mesh scales of the overlapping grids consistent so that accurate interpolation between the two grids can be performed. Fig. 2 shows a simple overlapping grid consisting of two component grids, an annular body grid ($G_B$) and a primary Cartesian grid ($G_P$). The primary domain is covered by the Cartesian grid $G_P$ and the domain close to the solid body is covered by the curvilinear grid $G_B$, which consists of the body surface (physical boundary), the interpolation boundary, and the periodic boundary. The interpolation boundary is located at an approximately constant distance from the body, and the periodic boundary is located between the rightmost points on the physical boundary and the interpolation boundary. For convenience of discussion, one quarter of the computational domain is marked and considered.

Fig. 2(a) shows the overlapping grid in physical space, while Figs. 2(b) and (c) show each component grid separately. In this particular example, the annular grid cuts a hole in the Cartesian grid so that the latter grid has a number of unused points marked by open circles. The other points on the component grids are classified as either discretization points (where the PDE or boundary conditions are discretized) or interpolation points. In addition, each boundary face of each component grid is classified as either a physical boundary (where boundary conditions are to be implemented), a periodic boundary or an interpolation boundary; one or more lines of ghost points are created for each component grid to aid in the application of boundary conditions.

Solution values at interpolation points of a grid $G_B$ are determined by interpolation from the donor points on another grid $G_P$. The donor points on grid $G_P$ are required to be either discretization points or interpolation points. Interpolation is performed in parameter space (unit-square coordinates). For each interpolation point on grid $G_B$,

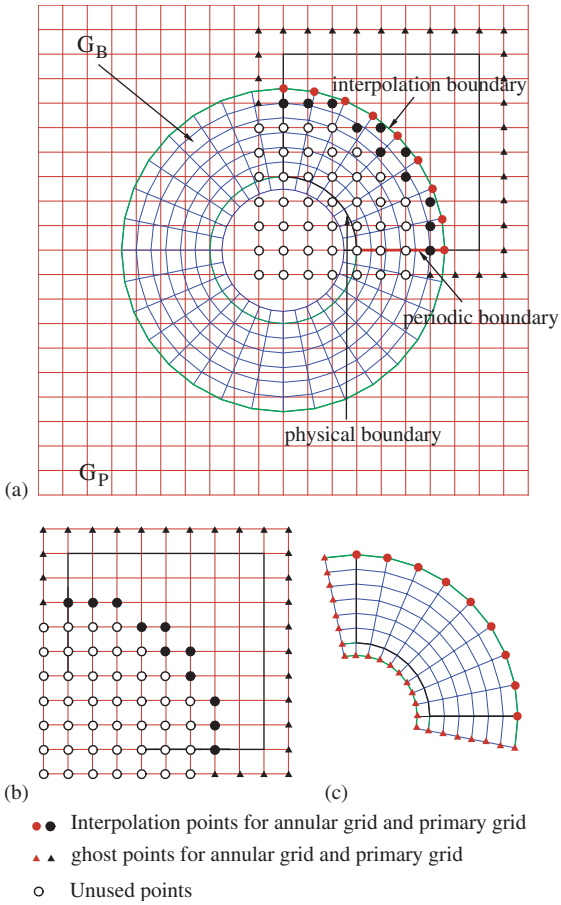


Fig. 2. Illustration of overlapping grid system and grid information exchange.

its parameter space coordinates on grid $G_P$ may be found using the inverse mapping from primary Cartesian coordinates. In parameter space, quadratic interpolation of second-order accuracy is used.

For a time-dependent grid system for the moving boundary problem, the moving object is treated artificially as a solid body and the grid points within the moving object are marked and excluded from the calculations at each time step, obviating the need for mesh regeneration.

### 3.2. Discretization

Let $\mathbf{V}_i$ and $P_i$ denote the discrete approximations to $u$ and $p$ so that

$$\mathbf{V}_i \approx \mathbf{u}(x_i), P_i \approx p(\mathbf{x}_i). \tag{3}$$

Here $\mathbf{V} = (V_{1i}, V_{2i})$ and $i = (i_1, i_2)$ is a multi-index. After discretizing in space the equations are of the form

$$\frac{\mathrm{d}}{\mathrm{d}t}\mathbf{V}_i + (\mathbf{V}_i \cdot \nabla_h)\mathbf{V}_i + \nabla_h P_i - \nu\Delta_h \mathbf{V}_i - \mathbf{f}(\mathbf{x}_i, t) = \mathbf{0}, \tag{4a}$$

$$\Delta_h \mathbf{P}_i + \sum\nolimits_m \nabla_h V_{m,i} \cdot \mathbf{D}_{m,h} V_i - C_{d,i}\nabla_h \cdot V_i - \nabla_h \cdot \mathbf{f}(\mathbf{x}_i, t) = 0, \tag{4b}$$

where the divergence damping coefficient, $C_{d,i}$ is defined below. The subscript $h$ denotes a second-order centered difference approximation

$$D_{m,h} \approx \frac{\partial}{\partial x_m}, \ \nabla_h = (D_{1,h}, D_{2,h}), \ \Delta_h \approx \sum\nolimits_m \frac{\partial^2}{\partial x_m^2}. \tag{5}$$

### 3.3. Divergence damping

The divergence damping term, $C_{d,i}\nabla_h \cdot \mathbf{V}_i$, appears in the pressure equation, Eq. (4b). In simplified terms, the coefficient $C_d$ is taken proportional to the inverse of the time step, $C_d \sim 1/\Delta t$. In practice it is found that $C_d \sim \nu/\Delta x^2$ can achieve better results. Detailed information about divergence damping can be found in Henshaw (2003).

### 3.4. Artificial diffusion

Henshaw (2003) gives the implementation of the second-order artificial diffusion shown as follows:

$$d_{2,i} = (\mathrm{ad21} + \mathrm{ad22}|\nabla_h V_i|_1) \sum_{m=1}^{n_d} \Delta_{m+}\Delta_{m-} V_i. \tag{6}$$

Typical choices for the constants are ad21 = 1 and ad22 = 0.5. Here $|\nabla_h V_i|_1$ is the magnitude of the velocity gradient and $\Delta_{m+}$ and $\Delta_{m-}$ are the forward and backward difference operators in direction $m$ respectively, and $n_d = 2$ in the present study.

$$|\nabla_h \mathbf{V}_i|_1 = n_d^{-2} \sum\nolimits_{m=1}^{n_d} \sum\nolimits_{n=1}^{n_d} |D_{m,h}\mathbf{V}_{ni}|, \tag{7a}$$

$$\Delta_{1+} V_i = V_{i_1+1} - V_i, \tag{7b}$$

$$\Delta_{1-} V_i = V_i - V_{i_1-1}, \tag{7c}$$

$$\Delta_{2+} V_i = V_{i_2+1} - V_i, \tag{7d}$$

$$\Delta_{2-} V_i = V_i - V_{i_2-1}, \tag{7e}$$

This form of the artificial diffusion is based on a theoretical result of Henshaw et al. (1989). The artificial diffusion is added to the momentum equations

$$\frac{\mathrm{d}}{\mathrm{d}t} V_i + (V_i \cdot \nabla_h) V_i + \nabla_h P_i - \nu\Delta_h V_i - f(x_i, t) - d_{2,i} = 0, \tag{8}$$

which does not affect the pressure equation.

## 4. Results and discussion

### 4.1. Validation

Flow past a pair of side-by-side identical circular cylinders is simulated by the present numerical algorithm and compared with the numerical results of Jester and Kallinderis (2003) and the experimental data of Chen (1987). The diameter of the two circular cylinders $D$ is 0.1 m. The computational domain (scaled with respect to the characteristic length $D$) is $20 \times 10$. The two circular cylinders are located at (6,4) and (6,6), respectively. Velocity fluctuations at the location P, (7,5) is measured (Fig. 3(a)). Uniform velocity profile $U_o = 3\,\mathrm{m/s}$ is imposed at the inflow boundary. The Reynolds number is 1000 in the present calculation.

Fig. 3(b) shows the velocity field around the cylinder pair. Two distinct vortex streets are coupled symmetrically, i.e. vortices are alternatively shed on the gap-side rather than the outside of the cylinders. The vortex streets can be clearly seen in pressure field around the cylinders (Fig. 3(c)). This symmetric formation and shedding of vortices observed in the present simulation agree well with the findings of Chen (1987) and Jester and Kallinderis (2003). However, the antisymmetric vortex formation pattern as observed by Williamson (1985) could not be reproduced here. Velocity fluctuation at the point P is shown in Fig. 3(d). Fourier analysis of the time-series velocity component $v$ is used to obtain the frequency $f$. The Strouhal number, defined as $\mathrm{St} = fD/U_o$, is calculated and yields a value of 0.24, which is comparable to the value of 0.26 obtained by Jester and Kallinderis (2003) for the coupled vortex streets.

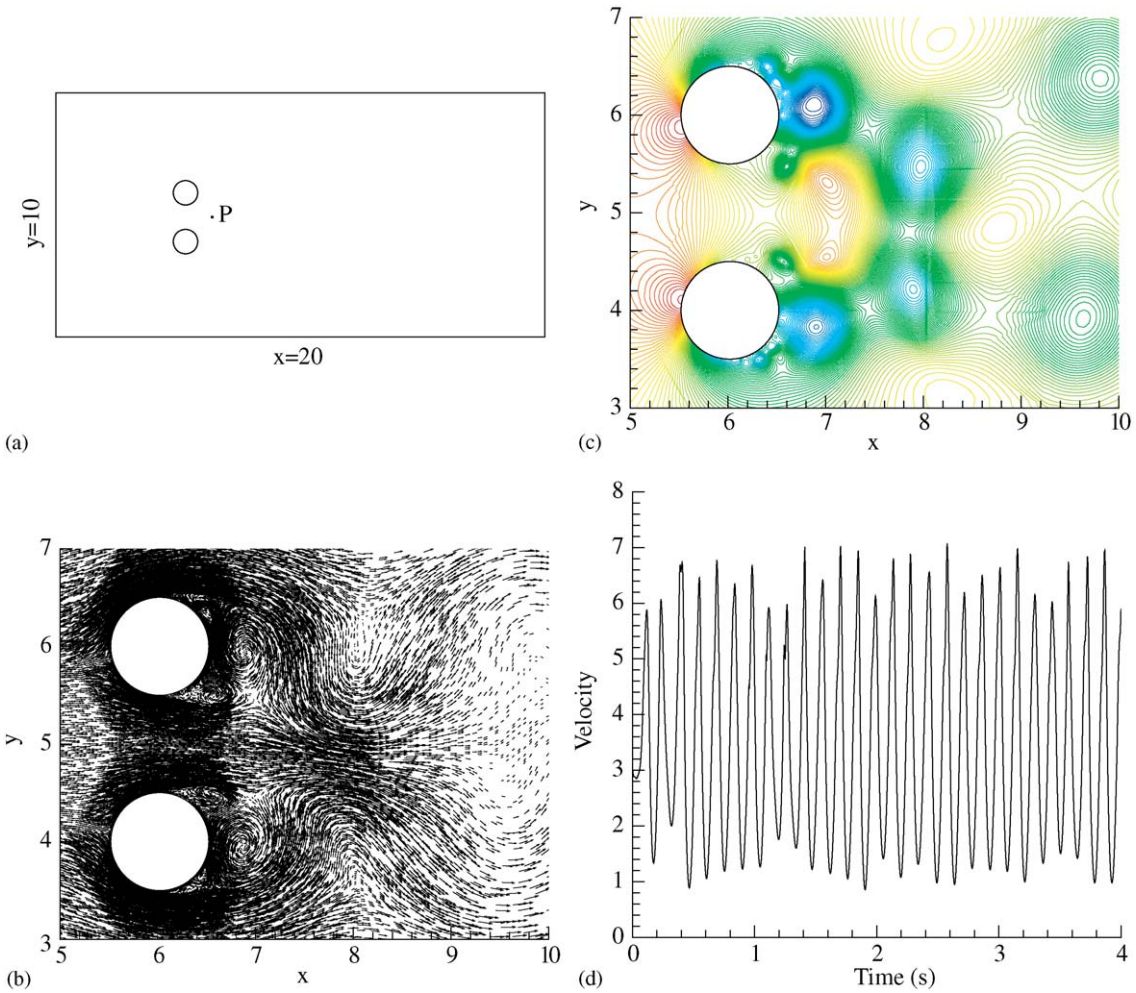


Fig. 3. Flow around a pair of identical circular cylinders: (a) computational domain; (b) velocity field around the cylinder pair; (c) pressure field around the cylinder pair; (d) velocity fluctuation at the monitoring point.

### 4.2. Street canyons with moving objects

Simulations were conducted for street canyons with two sets of objects, either circular or rectangular in shape with diameter or width equal to $D$. The Reynolds number based on the maximum inflow velocity $U_o$ at symmetric line and the characteristic length $D$ was $1.0 \times 10^4$. The flow is monitored at two locations A(0,1) and B(1,1) in the moving reference frame with its origin at the center of the moving object (Fig. 1). The velocity profile along the symmetry line and these two monitoring points in the wake area were studied.

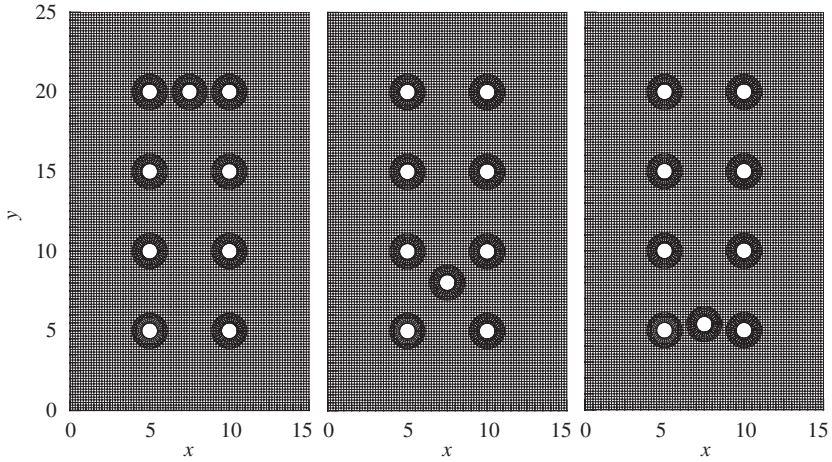


Fig. 4. Computational mesh for the circular cylinders at different time instants.

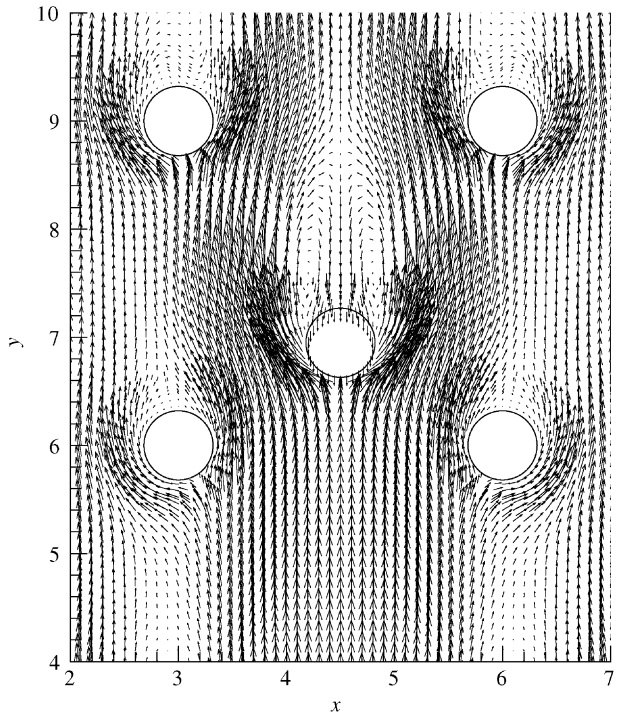


Fig. 5. An instantaneous velocity field around moving circular cylinder and its surroundings.

*4.2.1. Circular objects*

Circular objects with diameter $D = 0.2$ m were used to simulate moving and stationary vehicles. The computation domain (scaled with respect to the characteristic length $D$) was 15 units in spanwise and 25 units in the streamwise direction. The moving circular object was initially located at (7.5, 20) in the domain and moved downwards along the symmetrical axis (against the wind) with a constant velocity (Fig. 4). The overlapping grid system contained $91 \times 151$ Cartesian mesh for the rectangular background and nine $33 \times 6$ nodes for the body-fitted component grid around each circular object. The interpolation boundary condition was used at the outer boundary of component grids. Three different scenarios were considered—one moving cylinder, two moving cylinders with separation $g = 2.5$, and two

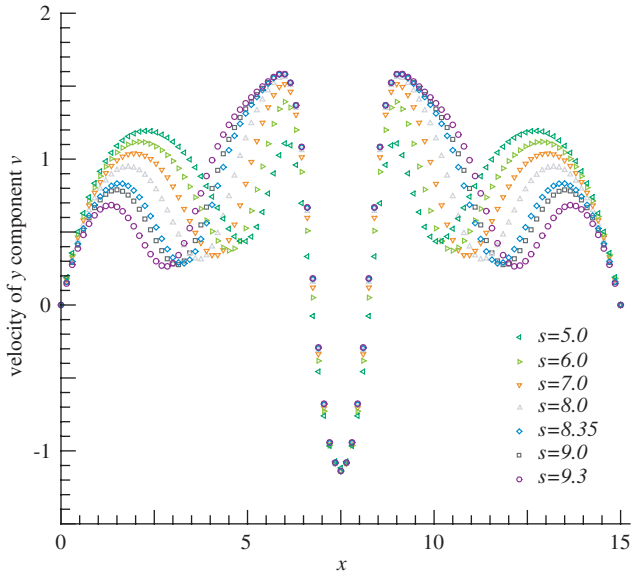


Fig. 6. Velocity profiles at $w = 0.5$ downstream of one moving circular cylinder with different building spaces $s$.

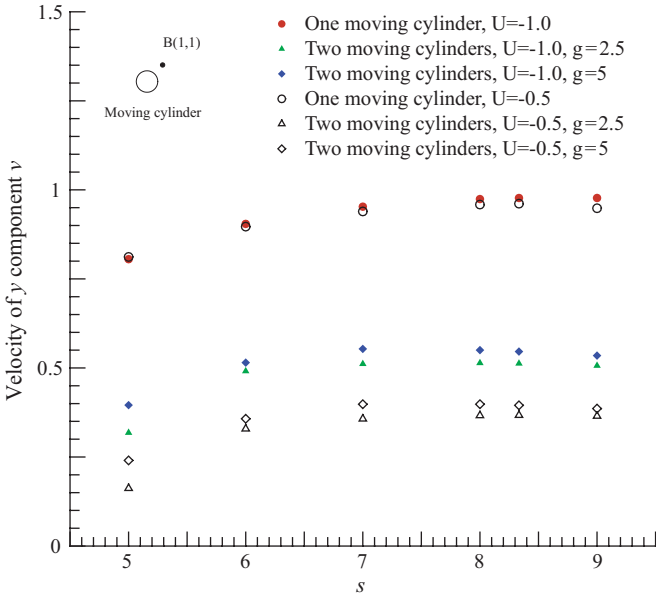


Fig. 7. Velocity at the monitoring point B in the wake of the moving circular cylinder under different scenarios.

moving cylinders with separation $g = 5$. Two different velocities, $U = -0.5$ and $-1$, of the moving object were adopted. The negative sign indicates that the object is moving against the wind direction, which is assumed to be the positive $y$-axis. The distance between the two columns of object array $s$, representing the distance between buildings, varied from 5 to 9 for each scenario.

The computational mesh at three instantaneous time steps is shown in Fig. 4. It should be noted that the mesh is not generated in each time step, but only interpolation between the overlapped regions is required, resulting in reduced CPU time. An instantaneous velocity field around the moving circular object is shown in Fig. 5. Velocity profiles at $w = 0.5$, where $w$ is the distance away from the stagnation point of moving cylinder, are shown in Fig. 6. It can be seen that the velocity right behind the moving object maintains a constant value despite the variation in $s$, while the velocity at the edge of the wake varies with $s$. It indicates that the flow velocity in the wake of the moving object is affected by its surrounding arrangement while the velocity in regions close to the moving object, e.g. at the monitoring point A, is determined by the velocity of the moving object. Fig. 7 summarizes the results for the velocity at the monitoring point B under six different scenarios. Based on the present simulation results, the flow velocity in the wake of the moving objects

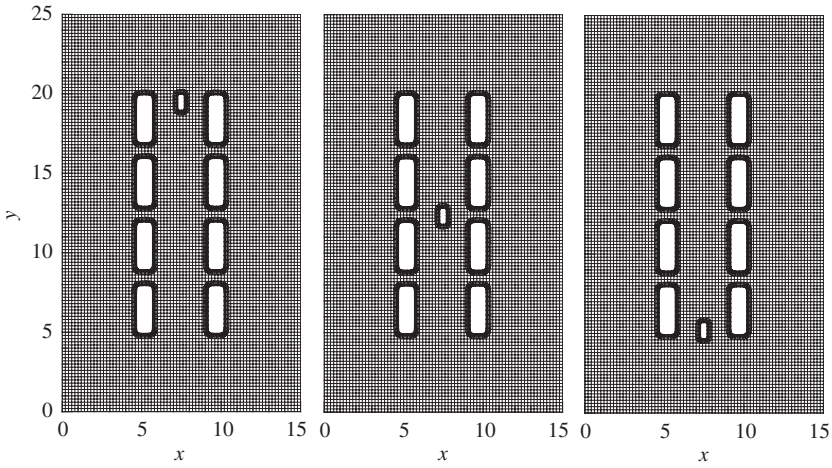


Fig. 8. Computational mesh for the rounded-rectangular cylinders at different time instants.

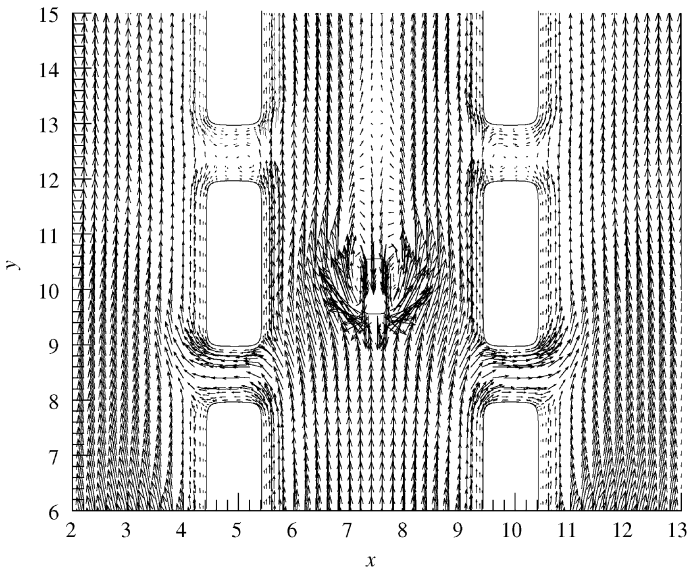


Fig. 9. Instantaneous velocity field around rounded-rectangular cylinders.

increases greatly when $s \leqslant 6$, and reaches a fairly constant value when $s > 6$. Velocity in the wake increases with the speed of the moving object. As a consequence, emissions from the moving objects have more momentum to transport. For the case of two moving objects, increasing separation results in higher velocity in the wake. This is due to the fact that the incident flow for the second moving object is in the wake of the object ahead.

*4.2.2. Rectangular objects*

Eight rounded-rectangular objects with width $1D$ ($= 0.2$ m) and length $3D$ were arranged in a $2 \times 4$ array in a computational domain, which is 15 wide and 25 long in nondimensional units. A smaller rounded-rectangular object, which is $0.4D$ wide and $1D$ long, was used to represent the moving vehicle (Fig. 8). The overlapping grid system included one $91 \times 151$ background grid and nine $33 \times 6$ component grids around each rounded-rectangular object. Interpolation boundary condition was used at the outer boundary of component grids. The centerline of the moving rounded-rectangular object moved along the symmetry axis at a constant velocity. Similar to the first set, moving velocity of the object is set as $U = -1$. The canyon width, i.e., the distance between the two columns of fixed objects array, $s$, varies from 3 to 9. Velocity profiles along the symmetry line for each simulation are investigated.

The computational mesh at three different time steps is shown in Fig. 8. An instantaneous velocity field around the rectangular object is shown in Fig. 9. Velocity profiles at $w = 0.5$ are analyzed using the same method as in group one. It is found that the velocity right behind the moving object maintains a constant value despite different $s$ values, while the velocity at the edge of the wake varies with the $s$ values.

Fig. 10 summarizes the velocity at the monitoring point B under the three different scenarios. Comparing with the simulations in group one, similar results can be found in this group. The flow velocity in the wake of the moving object increases with the separation between the two rounded-rectangular columns when $3 \leqslant s \leqslant 6$, and reaches a fairly constant value when $s > 6$. It is noted that the magnitude of the velocity in the wake of the moving rounded-rectangular cylinder is lower than that of the circular cylinder case. The blunt shape of the moving cylinder may be the cause of this phenomenon. Velocity in the wake increases when the speed of the moving cylinder becomes higher. When two moving cylinders are considered, increasing the separation will result in a higher velocity in the wake, which is similar to the results for the circular objects case. The velocity will be recovered when the distance to the moving object is increased. The centerline velocity profiles in the wake of the moving cylinders with different spaces $s$ are plotted, as shown in Fig. 11. The velocity in the recirculation region decreases exponentially as the distance from the moving object increases, till zero velocity is experienced, where the downstream distance is 2 units away from the moving vehicle, which indicates wake extension in the streamwise direction. It is interesting to see that the wake extensions almost keep constant despite of different $s$ values. For the flow velocity downstream of the recirculation region, which means the downstream distance to the moving cylinder is larger than 2 units, different behaviors at different $s$ values are found. For $s = 3.0$, the velocity reaches a constant value and is about 10% of the free-stream velocity due to the constraints of surrounding objects. For $s = 3.5$, velocity in the far wake along the symmetric line is about 50% of the free-stream flow.

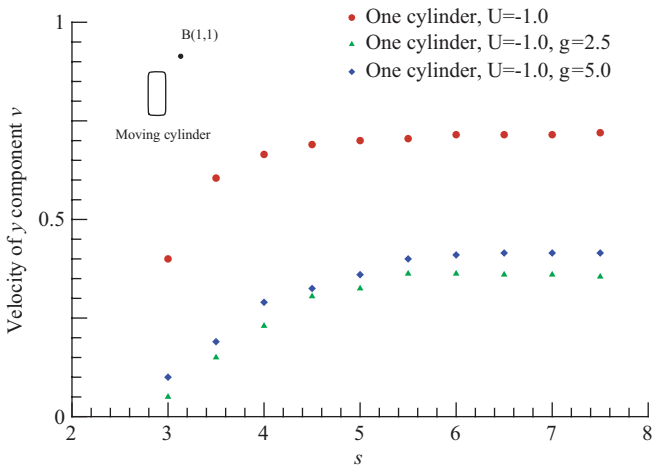


Fig. 10. Velocity at the monitoring point B in the wake of the moving rounded-rectangular cylinder under different scenarios.

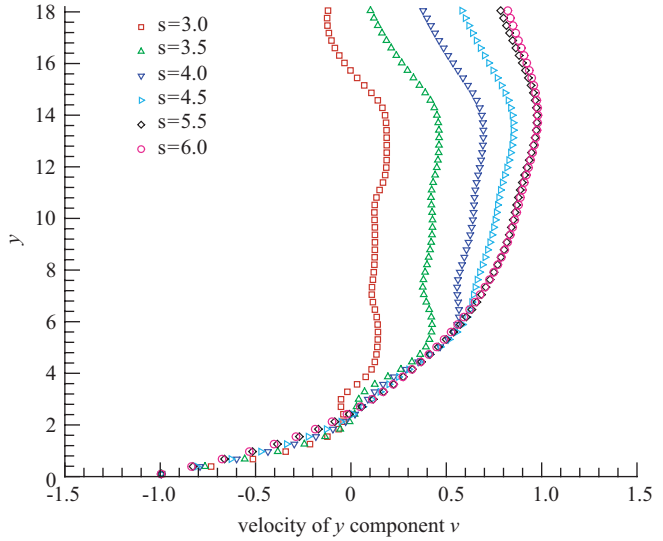


Fig. 11. Distribution of $y$ component velocity along the symmetric line downstream the moving rounded-rectangular cylinders.

For $s \geqslant 6$, the flow velocity along the symmetric line in the far-wake of the moving objects increases exponentially with increasing downstream distance and approaches the free-stream velocity when the distance is 14 downstream of the moving objects. It should be noted that the sudden change in velocity along the symmetry line is caused by the discontinuity in the placement of surrounding objects. These findings are consistent with the previous theoretical study of Eskridge and Hunt (1979).

## 5. Conclusions

A numerical method involving an overlapping grid procedure was implemented for simulating street canyon flow-fields with moving objects. The method was first verified with the case of flow past a pair of circular cylinders. Both the computed flow pattern and Strouhal number agreed well with the results in the literature. The numerical method was then applied to simulate flows around moving objects in street canyons with a Reynolds number of $10^4$. The present study focused on the horizontal flow around moving objects with different distances to the surrounding objects. The understanding of the relationship between the street canyon width and the flow field, and eventually the pollutant concentration due to the vehicular emissions is important to city planners, from the point of view of environmentally friendly design. It is observed that in the near-wake (recirculation region) of the moving object, the absolute value of velocity increases exponentially with distance away from the moving object and vanishes at the near-wake edge (wake stagnation point). For a given velocity of the moving object, the linear streamwise extent of the near-wake remains constant for values of the canyon width, $s$, (scaled with respect to the width of the moving object) less than 6. However, the velocity at the symmetric line in the far-wake (downstream of the recirculation region) is found to be a function of the canyon width. For a narrow street canyon, for example $s = 3$, the average far-wake velocity is about 10% of the free-stream velocity, and for $s = 3.5$, it is about 50% of the free-stream velocity; for $s \geqslant 6$, it increases exponentially with downstream distance away from the moving object. Simulations showed that away from the wake symmetry line the velocity increases with increasing $s$ from 3.0 to 6.0 and reaches a fairly constant value for $s > 6$.

The effectiveness of the overlapping grid procedure for simulating the flow field of a street canyon with moving objects has been demonstrated. Although the assumption of a two-dimensional laminar flow is not realistic at this Reynolds number as both three-dimensional effects and turbulence are significant, the present study can give a good insight of some basic physical phenomena present in real applications, as pointed out by Mittal et al. (1997) who also performed numerical simulation of laminar flows at $\mathrm{Re} = 1000$. Furthermore, it provides the first building block for the construction of an effective and efficient predictive methodology for the complex and more realistic configurations of street canyons.

## Acknowledgments

The first and second authors wish to acknowledge the Hong Kong Research Grant Council for supporting the project (HKU 7196/03E).

## References

Ahmad, K., Khare, M., Chaudhry, K.K., 2002. Model vehicle movement system in wind tunnels for exhaust dispersion studies under various urban street configurations. Journal of Wind Engineering and Industrial Aerodynamics 90, 1051–1064.

Baker, C.J., 2001. Flow and dispersion in ground vehicle wakes. Journal of Fluids and Structures 15, 1031–1060.

Beaton, J.L., Ranzieri, A.J., Shirley, E.C., Skog, J.B., 1972. Mathematical approach to estimating highway impact on air quality. Federal Highway Administration Report No. FHWA-RD-72-36, Washington, DC, USA.

Chen, S.S., 1987. Flow-induced Vibration of Circular Cylindrical Structures. Hemisphere, Washington.

Eskridge, R.E., Hunt, J.C.R., 1979. Highway modeling part 1. Prediction of velocity and turbulence fields in the wake of vehicles. Journal of Applied Meteorology 18, 387–400.

Eskridge, R.E., Thompson, R.S., 1982. Experimental and theoretical study of the wake of a block-shaped vehicle in a shear-free boundary flow. Atmospheric Environment 16, 2821–2836.

Henshaw, W.D., 1994. A fourth-order accurate method for the incompressible Navier–Stokes equations on overlapping grids. Journal of Computational Physics 113, 13–25.

Henshaw, W.D., 2003. OverBlownINS: The Incompressible Navier–Stokes Solver in OverBlown. http://www.llnl.gov/casc/Overture.

Henshaw, W.D., Kreiss, H.O., Reyna, L., 1989. On the smallest scale for the incompressible Navier–Stokes equations. Theoretical and Computational Fluid Dynamics 1, 65–95.

Jester, W., Kallinderis, Y., 2003. Numerical study of incompressible flow about fixed cylinder pairs. Journal of Fluids and Structures 17, 561–577.

Liu, C.H., Leung, D.Y.C., Barth, M.C., 2005. On the prediction of air and pollutant exchange rates in street canyons of different aspect ratios using large-eddy simulation. Atmospheric Environment 39, 1567–1574.

Mittal, S., Kumar, V., Raghuvanshi, A., 1997. Unsteady incompressible flows past two cylinders in tandem and staggered arrangements. International Journal for Numerical Methods in Fluids 25, 1315–1344.

Theodoridis, G., Moussiopoulos, N., 2000. Influence of building density and roof shape on the wind and dispersion characteristics in an urban area: a numerical study. Environmental Monitoring and Assessment 65, 407–415.

Vardoulakis, S., Fisher, B.E.A., Pericleous, K., Flesca, N.G., 2003. Modelling air quality in street canyons: a review. Atmospheric Environment 37, 155–182.

Williamson, C.H.K., 1985. Evolution of a single wake behind a pair of bluff bodies. Journal of Fluid Mechanics 159, 1–18.

Xia, J.Y., Leung, D.Y.C., 2001a. Numerical study on flow over buildings in street canyon. Journal of Environmental Engineering 127, 369–376.

Xia, J.Y., Leung, D.Y.C., 2001b. Pollutant dispersion in urban street canopies. Atmospheric Environment 35, 2033–2043.

Xia, J.Y., Leung, D.Y.C., 2001c. A concentration correction scheme for Lagrangian particle model and its application in street canyon air dispersion modelling. Atmospheric Environment 35, 5779–5788.

Zimmerman, J.R., Thompson, R.S., 1975. User's Guide for HIWAY, a highway air pollution model. EPA-650/4-74-008.